

Effect of molecular weight and density of ambient gas on shock wave in laser-induced surface nanostructuring

Liyang Guo and Xinwei Wang¹

Department of Mechanical Engineering, 2010 H M Black Engineering Building, Iowa State University, Ames, IA 50011-2161, USA

E-mail: xwang3@iastate.edu

Received 31 July 2008, in final form 10 October 2008

Published 12 December 2008

Online at stacks.iop.org/JPhysD/42/015307

Abstract

This paper presents the results of molecular dynamics studies about the shock wave during laser-induced surface nanostructuring. A quasi-three dimensional model is constructed to study systems consisting of over 2 million atoms. Detailed studies are carried out about the shock wave front and Mach number, evolution of plume and ambient gas interaction zone, and energy exchange between the ambient gas and plume. Under an ambience of lower pressure or lighter molecular mass, the plume affects a larger area while the strength of the shock wave front is weaker. With the same ambient pressure, the ablated material features the same kinetic energy at the late stage regardless of the molecular weight of the ambient gas. The same conclusion holds for the energy increase of the ambient gas as well. When the ambient pressure is reduced, more kinetic energy is carried out by the ablated material while less energy is transferred to the ambient gas. It is observed that heavier ambient gas could bounce back the ablated material to the target surface.

(Some figures in this article are in colour only in the electronic version)

1. Introduction

Conventional maskless manufacturing techniques are restricted by the diffraction limit. As an alternative, one has to use extreme UV radiation (10–100 nm) or soft x-rays to manufacture structures in the nanometre range [1]. A number of techniques have been developed to extend the resolution limit and provide tools and ultrasmall optoelectronic devices for nanomanufacturing such as nanofabricating, nanolithography and nanomodification [2–10]. Near-field scanning optical microscope (NSOM) works with resolutions from 10 to 100 nm with apertures and 1 to 20 nm without apertures [11–13]. The superlens is capable of imaging features with 60 nm or 1/6 of the illumination wavelength [14]. As one approach that attracted enormous interest in the past decade, the laser-assisted scanning probe microscope (SPM) has been shown to be effective for processing materials and surface at nanoscales. When irritated by a pulsed laser, the SPM tip could create a

significantly enhanced optical field with two orders of magnitude [15] enhancement. With a femtosecond laser, a resolution down to 10 nm could be achieved [16]. Using an atomic force microscope (AFM) combined with a 532 nm pulsed laser, surface structure with a lateral resolution of 1.5–7 nm has been created [17].

During the process of laser-assisted SPM nanostructuring, intensive laser heating will make the solid-state material transfer directly into the gas phase to result in phase explosion as a consequence of insufficient time for normal boiling to take place [18]. This often leads to a shock wave when an ambient gas is present during the process. Owing to the increasing interest in nanomanufacturing, there have been studies on properties of the expansion plume and its strong interactions with the ambient gas, analytically, experimentally and numerically. In Zhang's work, a one-dimensional model was established to describe the shock wave front [19]. Jeong *et al* [20] investigated the correlation between the transit time and location of the laser-induced shock wave and compared the conversion efficiency with the conventional blast wave.

¹ Author to whom any correspondence should be addressed.

Kohen and Martens [21] simulated the process of a pump laser exciting an impurity molecule embedded in a solid host to a repulsive electronic state. Their work provided a direct view of the generation and propagation of nanoscale shock waves.

In nanostructures, thermal movements of molecules/atoms show strong statistical variations in space since the equilibrium state cannot be established. Molecular dynamics (MD) simulation, which directly tracks the movements of molecules/atoms, is capable of exploring physical phenomena down to molecular/atomic levels. Wang's previous work explored the thermal and mechanical phenomena beneath the sample surface by tracking over 200 million atoms [22] and studied the solidification and epitaxial regrowth in surface nanostructuring [23]. Feng's work on nanodomain shock wave was focused on the interface properties of the shock wave front during its propagation [24]. However, none of the previous studies gives consideration of the effects of the molecular weight and density of ambient gas on shock wave in laser-induced nanostructuring.

In this paper, MD simulations are conducted to track the trajectory of over 2 million atoms. The evolution of the interaction zone and energy exchange between the plume and the ambient gas are studied with respect to different gas/solid molecular mass ratios and different ambient gas densities. The evolution of shock wave front position as well as velocity and Mach number in different ambient gases are also studied.

2. Methodologies of simulation

The modelled system is an argon thin film positioned in a gas environment. Initially, the system is equilibrated at the designated temperature 50 K for 200 ps. A pulsed laser is then focused on the centre of the film for 30 ps. The process is recorded from the beginning until 1 ns. The objective is to investigate the effect of the molecular weight and density of ambient gas on the laser-induced shock wave. Eight cases are studied in two groups. Group one has the same ambient gas pressure but different molecular mass ratios of gas to solid. This is designed to reflect the effect of environment molecular mass on the shock wave rather than to recover a practical experimental condition. Group two uses the same ambient gas molecular weight but different ambient gas pressures. For ease of discussion, β is used to represent the molecular mass ratio of gas to solid, which has the form of $\beta = M_{\text{gas}}/M_{\text{solid}}$, where M_{gas} and M_{solid} are the molecular mass of the ambient gas and the target solid. γ represents the ratio of the ambient gas pressure to a reference pressure (0.217 MPa), which is expressed as $\gamma = p_{\text{ambient}}/p_{\text{ref}}$.

A modified quasi three-dimensional domain from our previous work is established in this study. The construction of the solid target in each case is basically 5 face-centred-cubes (FCCs) in the x direction, 1700 or 1664 FCCs in the y direction and 60 FCCs in the z direction for group 1, and 1664 FCCs in the y direction and 64 FCCs in the z direction for group 2. The lattice constant for each FCC cell is 5.414 Å.

In MD simulation, the dynamics of the system are governed by the classical Newtonian equation $m_i d^2 r_i / dt^2 = \sum_{j \neq i} F_{ij}$, where m_i and r_i are the mass and position of atom i , respectively, F_{ij} is the pair force between atoms i and j , which

is calculated as $F_{ij} = -\partial \phi_{ij} / \partial r_{ij}$. The Lennard-Jones (12-6) potential is used to calculate the force between atoms $\phi_{ij} = 4 \cdot \epsilon [(\sigma/r_{ij})^{12} - (\sigma/r_{ij})^6]$, where for argon $\epsilon = 1.653 \times 10^{-21}$ J is the LJ well depth parameter, $\sigma = 3.406$ Å is referred to as the equilibrium separation parameter, and $r_{ij} = r_i - r_j$. In this calculation a time step of 25 fs is used. The Newtonian equation is solved by applying the Verlet algorithm to velocity [25]. The interactions between atoms are truncated at the cutoff distance (2.5σ), beyond which the interactions are negligible. In this work, only the repulsive force is considered between atoms in the ambient gas. The solid and gas atoms share the same molecular mass and repulsive potential for group 2 studies. For group 1 studies, the ambient gas shares the same repulsive potential as the target, but has reduced molecular weight. The initial ensemble momentum is subtracted at the beginning of simulation to keep the total momentum zero. Computation of the force between an atom and its neighbours is arranged by the cell structure and linked-list methods [25].

The simulation is based on a MD program package developed by our group using FORTRAN. To reduce the computational time, the programs are further modified using message passing interface to realize parallel computation. As a result, the computational time for each step is about 7 s by employing 4 processors, which is almost 1/4 the time required if only one processor is used for computation. Figure 1 illustrates the schematic of the parallel computation. The whole domain is divided evenly into 4 sub-domains in the y direction. Each sub-domain is computed by one processor. At every time step, each processor will do self-diagnosis at its right and left boundaries. If one atom moves out of the boundary limit of the present sub-domain, it will be excluded from the present one and passed to its physical neighbour. So each processor will exchange atoms with its neighbours every time step. For the left and right boundaries of the whole domain, periodical boundary conditions are applied to deal with those atoms that may move out of the computational space. This means the atoms excluded from processor 4 will enter processor 1. Under this condition, the total number of tracked atoms remains constant. In this simulation, the domain size in the y direction is designed to keep the shock wave movement within the domain as much as possible.

The work done by our laboratory has proved that the physical model used in this work makes the ambient gas very close to the ideal gas situation [24]. This is due to the large spacing among gas atoms and the weak interaction between them. The pressure and sound speed based on the ideal gas model for the simulated cases in this work are summarized in table 1. The density of the ambient gas used in pressure evaluation is calculated using the total number of gas atoms and the gas domain size in our MD simulation.

The laser beam follows the Gaussian distribution in space and time domains

$$I = I_0 \exp\left(-\frac{(\vec{r} - \vec{r}_0)^2}{r_g^2}\right) \cdot \exp\left(-\frac{(t - t_0)^2}{t_g^2}\right), \quad (1)$$

where I_0 is a laser beam intensity constant, r is the location of the laser beam, r_0 the centre of the beam, r_g the size constant of

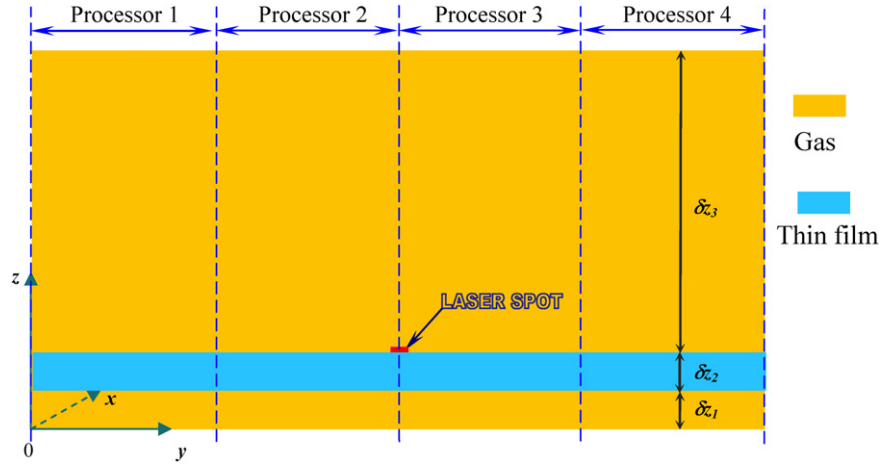


Figure 1. Schematic of the MD configuration for shock wave study and parallel computation (domain sizes under different conditions are listed in table 3).

Table 1. Sound speed and pressure under ideal gas assumption.

Group	Conditions	Pressure (MPa)	Sound speed (m s ⁻¹)
1	$\beta = 2, \gamma = 1$	0.217	93
	$\beta = 1, \gamma = 1$	0.217	132
	$\beta = 0.5, \gamma = 1$	0.217	186
	$\beta = 0.25, \gamma = 1$	0.217	263
	$\beta = 0.125, \gamma = 1$	0.217	373
2	$\beta = 1, \gamma = 0.25$	0.0543	132
	$\beta = 1, \gamma = 0.0626$	0.0136	132
	$\beta = 1, \gamma = 0.0157$	0.0034	132

Table 2. Values of the parameters used in the simulation.

Parameter	Value
ε , LJ well depth parameter	1.653×10^{-21} J
σ_e , LJ equilibrium separation	3.406 Å
m , Argon atomic mass	66.3×10^{-27} kg
k_B , Boltzmann's constant	1.38×10^{-23} J K ⁻¹
a , Lattice constant	5.414 Å
r_c , Cutoff distance	8.515 Å
τ , Laser beam absorption depth	10 nm
$\delta\tau$, Time step	25 fs
I_0	3.74×10^{12} W m ⁻²
r_g	2 nm
t_0	10 ps
t_g	3 ps

the laser spot, t the laser heating time, t_0 the peak location of the laser in the time domain and t_g the characteristic time of the laser pulse width. Values of the parameters used in this work are summarized in table 2.

The laser energy transmission in materials obeys the Lambert law $I = -I dz/\tau$, where I is the laser beam intensity, τ the absorption depth and z the coordinate in the laser incident direction. The absorption depth is dependent on the material and laser wavelength. When conducting the simulation, 10 nm is used as the value of τ . This arbitrary value is chosen to reflect the fact of volume absorption in the material rather than to represent a realistic experimental condition.

Figure 2 shows the schematic of the laser beam absorption in the material. The laser energy absorbed by atoms within each time step for cell 1 is

$$\delta E_1 = E_1[1 - \exp(-\delta z/\tau_1)], \quad (2)$$

where δz is the size of cells in the z direction. In MD simulation, δz (cell size) is chosen to be a little larger than the cutoff distance (2.5σ) in order to use the linked-list method. The actual absorption depth in cell 1 is adjusted as $\tau_1 = \tau \cdot \rho_0/\rho_1$ with ρ_1 the density of atoms in cell 1 and ρ_0 the density of argon at 50 K. The incident laser energy on the adjacent cell below cell 1 will be $E_1 - \delta E_1$, and so on to the next cell. The energy absorption is achieved by scaling the velocity of atoms in each cell. Details were discussed in Wang's previous work [22].

3. Results and discussion

The dimensions of the domain for each case are 2.707×920.38 (or 900.89×595.54 nm³ ($x \times y \times z$)) for group 1 and $2.707 \times 900.89 \times 1801.78$ nm³ for group 2 (listed in table 3). The total number of atoms in the computational domain is also summarized in table 3. The pulsed laser energy is 0.25 fJ (fJ=10⁻¹⁵ J), and the pulse width is 5 ps full width at half maximum (FWHM) (table 2). For the optical absorption depth used in this work (10 nm), the target material is thick enough to have sound absorption of the laser energy. We have conducted different simulations and found that for thinner target materials (e.g. 20 nm), some of the laser energy will pass through the target. Additionally, the strong recoil pressure in laser ablation will bend thin targets to introduce unrealistic physical phenomena. The size of the target used in this work is chosen to have a large absorption of the laser energy while reducing the computational time as much as possible. Thicker targets (e.g. 60 nm) have been used in our MD modelling of laser-induced surface nanostructuring and no appreciable difference is observed in comparison with the results using films 30 nm thick [26].

Shown in figure 3 are the snapshots of the simulated systems at different instants. The blue and red dots represent

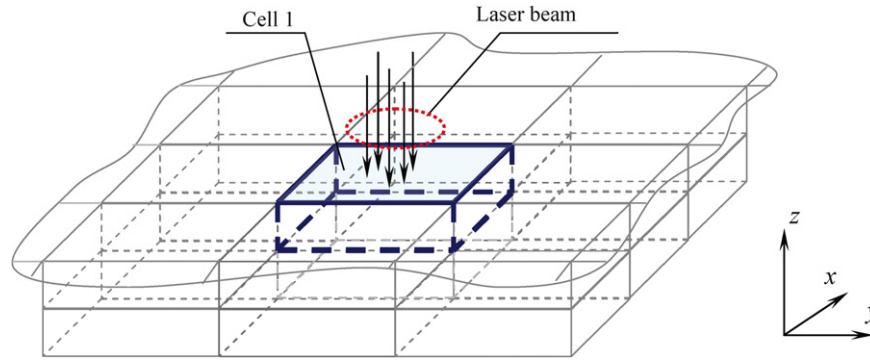


Figure 2. Schematic of the laser beam absorption in the material.

Table 3. Conditions, domain sizes and total number of atoms for different groups.

Group	Conditions	δz_1 (nm)	δz_2 (nm)	δz_3 (nm)	l_x (nm)	l_y (nm)	N
1	$\beta = 2, \gamma = 1$	21.656	32.484	541.4	2.707	920.38	2480 960
	$\beta = 1, \gamma = 1$	21.656	32.484	541.4	2.707	920.38	2480 960
	$\beta = 0.5, \gamma = 1$	21.656	32.484	541.4	2.707	920.38	2480 960
	$\beta = 0.25, \gamma = 1$	21.656	32.484	541.4	2.707	920.38	2480 960
	$\beta = 0.125, \gamma = 1$	21.656	32.484	541.4	2.707	900.89	2429 440
2	$\beta = 1, \gamma = 0.25$	34.650	34.650	1732.479	2.707	900.89	2469 376
	$\beta = 1, \gamma = 0.0626$	34.650	34.650	1732.479	2.707	900.89	2214 784
	$\beta = 1, \gamma = 0.0157$	34.650	34.650	1732.479	2.707	900.89	2151 136

δz_1 : ambient gas thickness below target film; δz_2 : target film thickness; δz_3 : ambient gas thickness above target film; l_x : domain size in the x direction; l_y : domain size in the y direction; N : total number of atoms within the domain.

ambient gas and target atoms, respectively. As mentioned above, the size difference in the z coordinate is due to the construction of the modelled system. And since the area below the film will not be influenced by the shock wave, only the area above the film and the top layer of the film is plotted out in each case. Particularly, for each snapshot in figure 3, the axis is 50–595 nm in the z direction and 0–900 nm in the y direction.

Figure 3 shows the formation and propagation of the shock wave front in space for five typical cases. As reported in the literature, the intensive laser heating causes the material to experience rapid phase change and explosion [18, 22]. The exploded material creates a plume which propagates into the ambient gas. The plume penetrates the ambient gas with a speed exceeding the local sound speed (table 1) that consequently forms a shock wave (figure 3). Because of the energy dissipation, the movement of target atoms will slow down but the gas wave will still exist and push the ambient gas to move [24]. A general trend observed in figure 3 is that under the same ambient pressure ($\gamma = 1$), when the ambient molecular mass is heavier (meaning denser ambient gas and higher β value), the shock wave moves slower, largely due to the strong constraint from the ambience which suppresses the phase explosion very much. When the pressure of the ambient gas gets lower (lower pressure and smaller γ value), the strength of the shock wave is weakened, and the shock wave becomes hard to distinguish ($\beta = 1, \gamma = 0.0626$). This is because the lower number density of atoms in the ambient gas leaves significant spacing for the ablated material to penetrate with little scattering. For the lowest pressure case ($\beta = 1,$

$\gamma = 0.0626$), no shock wave is observed. The ablated atoms penetrate into the ambient gas and mix with them.

3.1. Evolution of shockwave front

To investigate the movement of the shock wave front, first the position and speed of ambient gas atoms and target atoms are calculated separately and plotted in space. Figure 4 shows the snapshots at 100, 400 and 800 ps for five different ambient gas molecular weights. The black dots and red dots represent the target and gas atoms; the blue and pink lines represent the velocity of ablated target atoms and ambient gas. Only the central part in the y direction with a size of about 17 nm (Δy) is used for this calculation. Basically, the velocity here does not represent the speed of shock wave front propagation, but is the mass velocity. As shown in these figures, the movements of both kinds of atoms are faster in lighter gas ambience. Comparison between the case ($\beta = 0.125, \gamma = 1$) and $\beta = 2, \gamma = 1$) at 100 ps strongly supports this argument. This is because when the ambient gas is lighter, it imposes less constraint on the ejected plume, leading to higher plume velocity. At 400 ps, the speed of target atoms in the case ($\beta = 0.5, \gamma = 1$) decays faster than in the case ($\beta = 1, \gamma = 1$), but the speed of ambient gas is higher than that in ($\beta = 1, \gamma = 1$). From the figures at 400 ps, it is clear that when a lighter ambient gas is present, the shock wave moves faster. At 800 ps, the wave formed by moving atoms disappears in the case ($\beta = 0.25, \gamma = 1$) and ($\beta = 0.125, \gamma = 1$). But in the case ($\beta = 0.5, \gamma = 1$), ($\beta = 1, \gamma = 1$) and ($\beta = 2, \gamma = 1$), the bulk movements of atoms in the ambient gas

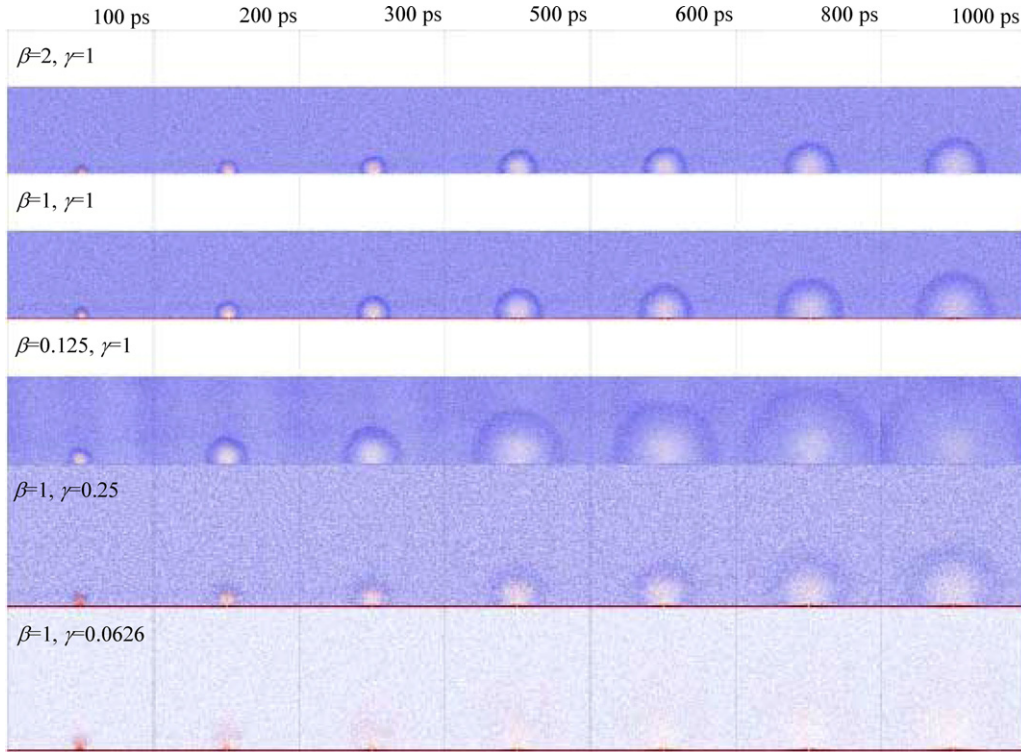


Figure 3. Evolution of atomic positions during shock wave formation and propagation (different cases at different time instants are listed in the column). Each dot in the figure represents an atom. Red dots: target atoms; blue dots: ambient gas atoms. Horizontal coordinate: y coordinate in the simulation (0–900 nm). Vertical coordinate: z coordinate in the simulation (50–595 nm). (Colour online.)

are still recognizable, which means the propagation will keep going.

To further investigate the shock wave phenomenon, we use three parameters: shock wave front position, propagation velocity and Mach number in an attempt to describe the movement of the shock wave front. The shock wave front position is estimated by direct observation of atomic snapshots in the direction normal to the target surface, where a density jump can be observed. The velocity is derived from $v = dz/dt$. The determination of Mach number (M) follows $M = v/v_s$, where v is the velocity of the shock wave front, v_s is the local sound speed, which is determined based on the ideal gas model. For monatomic gases, v_s is calculated using the following formula:

$$v_s = \sqrt{\gamma k_B T / m_o}, \quad \text{with } \gamma = c_p / c_v = (c_v + R) / c_v$$

$$\text{and } c_v = 3/2R, \quad (3)$$

where γ is the adiabatic index, R the universal gas constant, m_o the atomic mass and T temperature. Table 1 lists the speed of sound calculated in this work.

For some cases, the interface between the shock wave front and the ambience is too vague to distinguish at long times (1 ns). For example, in the case ($\beta = 0.125, \gamma = 1$) the shock wave front almost disappears at 400 ps. For the case ($\beta = 2, \gamma = 1$), from 0 to 30 ps the shock wave front only propagates a very short distance and is difficult to distinguish. To suppress the statistical uncertainty, the position in this case is recorded starting from 30 ps. Shown in figure 5 are the shock wave front position and velocity against time. The symbols are the observable front position (MD simulation),

and the solid lines are the fitting curve of the position data in figure 5(a). It is observed that the molecular mass of the ambient gas has significant impact on the shock wave propagation speed. At the beginning, the front propagates with a speed of up to 1200 m s^{-1} . But the movement decays quickly as the shock wave front is constrained by the stationary ambient gas. The decay slows down and the shock wave front reaches a relatively steady speed after some time. This time is different for each case from about 250 to 550 ps. For lighter ambient gas, the shock wave front movement can be quite steady after 200 ps ($\beta = 0.125, \gamma = 1$) while for heavier ambient gas, the movement of the shock wave decays till 550 ps. For heavier gas environment, the propagation is sluggish but will last a longer time. The movement in lighter ambience could reach a speed of up to 1200 m s^{-1} , but does not last long.

The evolution of Mach number under different molecular mass ratios is shown in figure 6. For the five cases, the ambient pressure is almost the same, around 0.217 MPa. At the early stage of shock wave development, the Mach number is higher in the case ($\beta = 2, \gamma = 1$) and ($\beta = 1, \gamma = 1$) followed by the case ($\beta = 0.5, \gamma = 1$), ($\beta = 0.25, \gamma = 1$) and ($\beta = 0.125, \gamma = 1$). At the late stage, the Mach number for all cases becomes almost the same. Although the shock wave front propagates faster in lighter ambient gases, the speed of sound increases, too. This explains why the Mach number differs little among these cases at the late stage of shock wave formation. After about 400 ps, the density jump at the shock wave front in the case ($\beta = 0.125, \gamma = 1$) becomes difficult to recognize. The ablated atoms stop moving forward at a

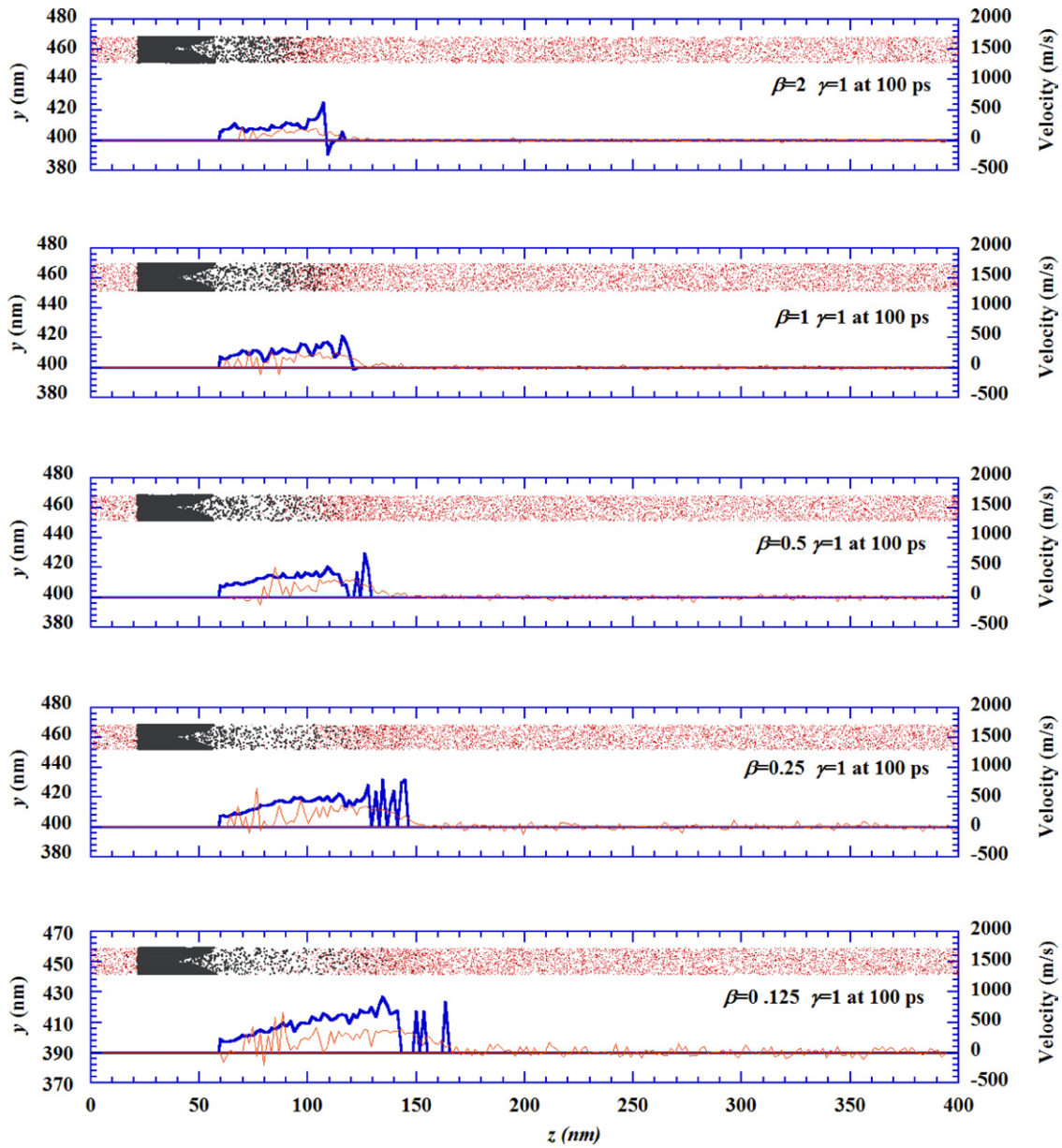


Figure 4. Movements of target atoms and ambient gas atoms (black dots and blue lines represent target atoms and their speed; red dots and pink lines represent ambient gas atoms and their speed). (Colour online.)

distance of around 250 nm. The energy of the shock wave will then be dissipated through the form of sound wave.

3.2. Evolution of the interaction zone

Once the shock wave forms, its interaction with the ambient gas is a very important phenomenon since such interaction can strongly influence the evolution of the plume and the nanoclusters inside. An interaction zone is defined above the film where the ejected target atoms interact strongly with the ambient gas atoms. In this section how the size of the interaction zone evolves during shock wave propagation is explored. Since the shock wave propagation occurs within a limited space, only the space above the film is considered. In order to exclude the melted target near the film surface, the starting calculation point is 61 nm in the z direction. Assuming

an area containing one or both of the target atoms and ambient atoms, the calculation takes the following three situations into consideration: if both the kinds of atoms have the same amount (number of atoms), this area is deemed as 100% for interaction; if the area contains only one kind of atoms, this area is deemed as 0% interaction; otherwise, the percentage of the area for interaction is dependent on the relative number of each kind of atoms in the area. To reflect the evolution of the interaction zone, this area is divided into small areas with 10 cells in the z and y directions. Integrating the interacting area over the whole domain of interest, using n_g and n_t to represent the number of ambient gas and target atoms, and A the area, the calculation of the total interaction zone area (A_{IZ}) at each time step is

$$A_{IZ} = \int_A \frac{4n_g n_t}{(n_g + n_t)^2} dA. \quad (4)$$

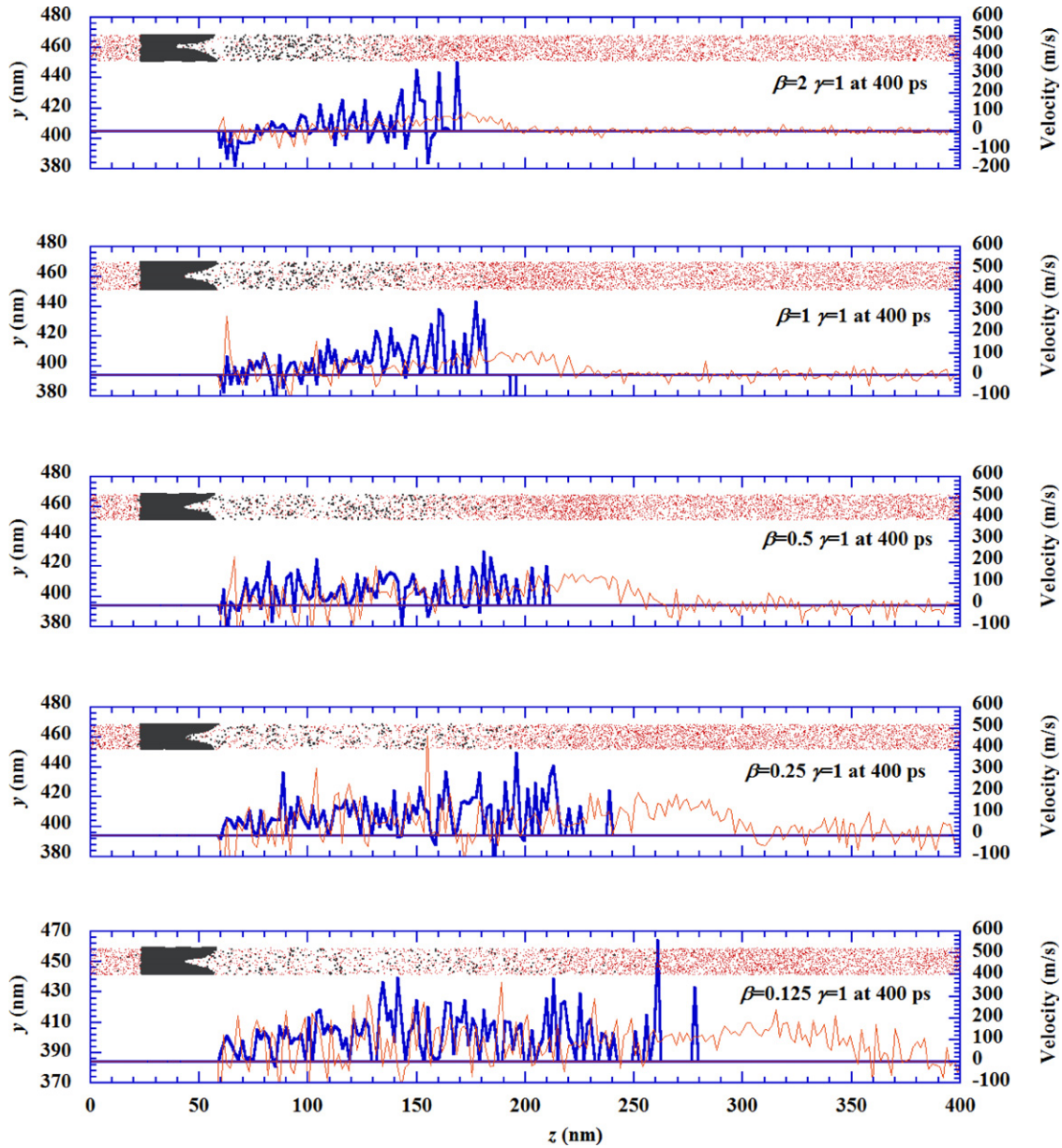


Figure 4. Continued.

dA is calculated as $dydz$, where dy and dz are the size of the discrete cell for interaction zone calculation. Selection of size for the discrete cell is critical to obtain physically reasonable results for the interaction zone. The size should be both sensitive and relatively stable to reflect the evolution of the interaction zone. If the cell is too small, large noise would be introduced. Results from too large cells cannot give any meaningful insights into the shock wave propagation. Figure 7 is the evolution of interaction zone area for different cases.

For different gas environment under the same pressure, the area of the interaction zone increases fast at the beginning, then slows down and reaches a stable value after some time. Here we define a full development time (FDT) to describe this period. It is expected that the interaction zone area will increase when β decreases since the speed of the shock wave is higher for smaller β . For each kind of gas, the FDT increases

as β increases. In the case ($\beta = 2, \gamma = 1$) it takes about 500 ps for the plume to fully develop and 250 ps for the case ($\beta = 0.125, \gamma = 1$). These time instants coincide with the time noticed in figure 5(b) when the movement of the shock wave fronts reach a relatively steady speed. The flat line after the FDT may suggest that the bulk movement of ejected atoms stops after the FDT. On the other hand, the shock wave front keeps propagating in the ambient gas. Figure 7 shows that for the cases of ($\beta = 0.125, \gamma = 1$) and ($\beta = 0.25, \gamma = 1$), there is a slight drop in the interaction zone area at the end of the simulation. This may result from the high speed of ejected target atoms which push the ambient gas atoms to move so fast that some of the atoms exceed the boundary in the z direction. Due to the periodical boundary conditions, the atoms will re-enter the computational domain from the opposite side, constrain the propagation of the shock wave and reduce the interaction zone area.

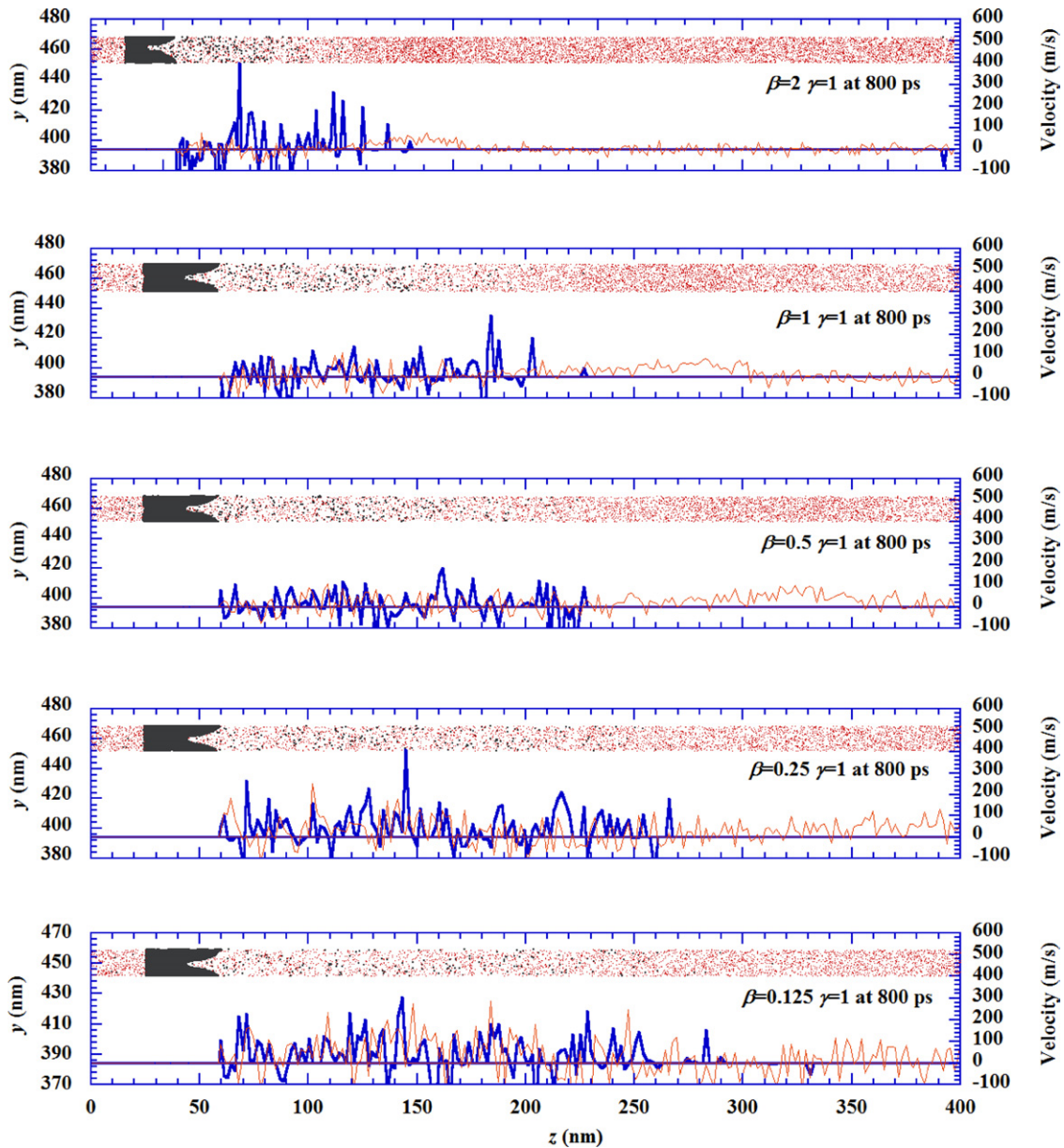


Figure 4. Continued.

For the same ambient gas at different pressures, figure 7 shows that as γ (pressure) decreases, the interaction zone area increases rapidly. This increasing speed is far higher than the area increasing speed in the case ($\beta = 1, \gamma = 1$) where the pressure is much higher. For ($\beta = 1, \gamma = 0.0157$) and ($\beta = 1, \gamma = 0.0626$) the plume propagates in space with little constraint since the atomic spacing in the ambient gas in these cases is very close to, or larger than the size of the laser spot. Therefore, the ablated materials (atoms, clusters) have a good chance to go through the atomic spacing in the ambience with little scattering. For ($\beta = 1, \gamma = 0.25$), the interaction zone area increases much slower than the cases of ($\beta = 1, \gamma = 0.0157$) and ($\beta = 1, \gamma = 0.0626$). At 600 ps, the interaction zone area for ($\beta = 1, \gamma = 0.0626$) becomes smaller than that for ($\beta = 1, \gamma = 0.25$) This could be due to the fact that ablated materials move faster for ($\beta = 1, \gamma = 0.0626$) and they move out of the computational domain and re-enter

from the opposite side. Such a phenomenon slows the mixing process between the ablated material and the ambient gas. The evolution of the interaction zone for the plume and the ambient gas suggests that the plume can affect a larger area in lower ambient pressure or lighter ambient gas, which has been observed in the experiment conducted by Edens *et al* [27].

3.3. Energy exchange between plume and ambient gas in the shockwave

During laser ablation, the laser energy will be dissipated in the film in the forms of phase change and stress wave, and through shock wave propagating in the ambient gas. Many studies have been conducted with respect to the absorption of laser energy during laser ablation. In this work, the energy exchange between the ablated target atoms and the ambient gas atoms is explored in an attempt to study the effect of ambient gas on

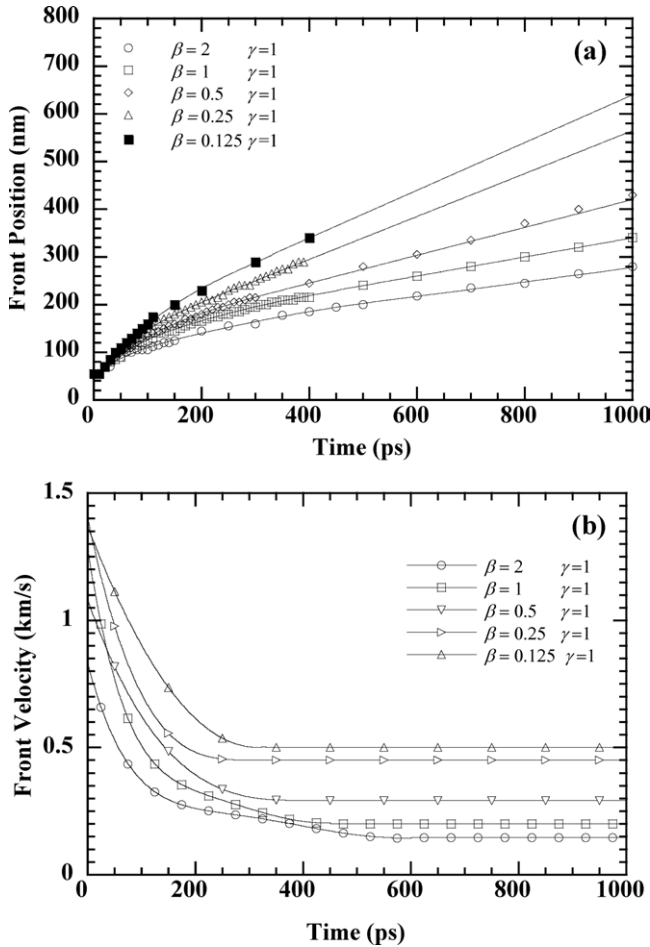


Figure 5. Shock wave front positions (a) and velocities (b) in different ambient gases. In figure (a), the solid lines are the fitting curve of the MD data.

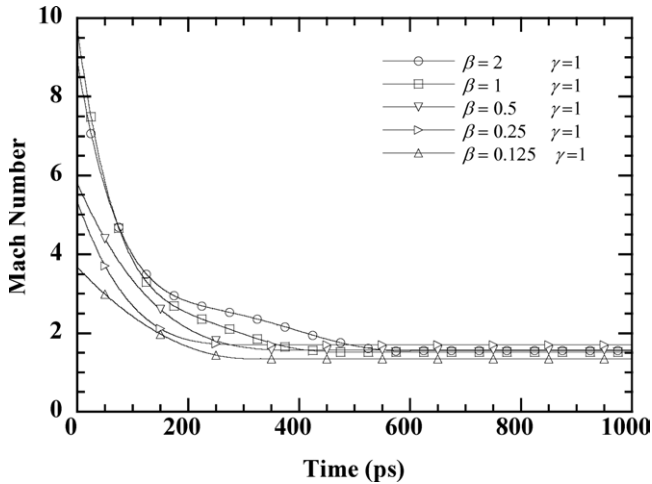


Figure 6. Decay of the Mach number of the shock wave front propagation in different ambient gases.

the energy exchange. The total kinetic energy of the ejected atoms and kinetic energy change of the ambient gas atoms are calculated separately for different β and γ . The results are plotted in figure 8. Under the same ambient pressure, it can be seen (figure 8(a)) that the energy increase in different ambient gases is about 2×10^{-17} J, regardless of the molecular mass.

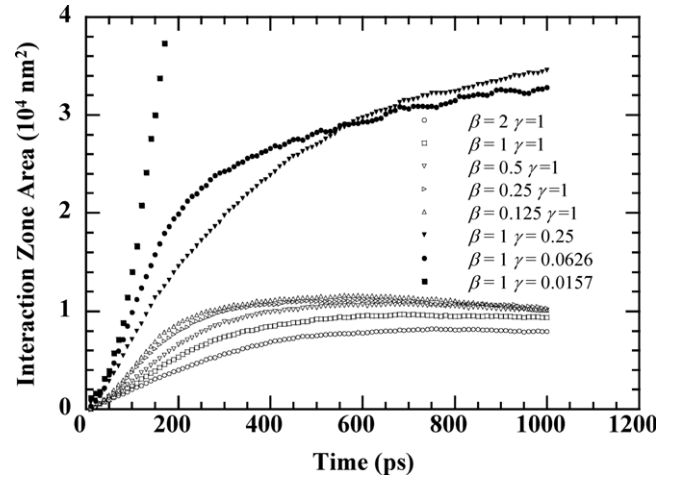


Figure 7. Evolution of the interaction zone area under the influence of different β and γ .

The energy of the ablated target atoms decreases as β increases during the early stage but reaches almost the same level after a while (figure 8(a)).

In the same gas ambience, the density jump at the shock wave front exists for the case ($\beta = 1, \gamma = 1$) but becomes invisible for ($\beta = 1, \gamma = 0.0626$) (figure 3). The curves of energy change for the ambient atoms (figure 8(b)) become less steep as γ decreases. For the case ($\beta = 1, \gamma = 0.0157$), the energy increase of the ambient gas has become almost linear with time. Under lower ambient pressure, it takes a longer time for the ambient gas to reach a steady energy state due to the rare scattering between the ablated target atoms and ambient atoms. Weaker energy increase in the ambient gas is attributed to the fact that no shock wave is observed in the case ($\beta = 1, \gamma = 0.0157$). The ablated atoms and the ambient gas atoms have very little interaction and energy exchange due to the large atomic spacing of the ambient atoms. The energy increase of the ambient gas is faster and higher in higher pressure environment. It is conclusive from figure 8(b) that more energy goes into the plume instead of the ambient gas in lower pressure gas environment.

According to the calculation, the higher ablation rate and lower energy exchange between the ejected target atoms and the ambient gas atoms can be a reason for the above phenomenon. By summing up the ablated target atoms in a designated area, the mass of ablated material is calculated and shown in figure 9. The results show that less ablated material is present in heavier ambient gases. For ($\beta = 2, \gamma = 1$) and ($\beta = 1, \gamma = 1$), there is an obvious decay in the material ablation after the peak value. From the snapshots in figure 3 it is seen that the plume under these conditions is still within the domain, which indicates no atoms flying out of the boundary. Therefore the reason for the ablation decay with time can be attributed to the fact that some of the ejected atoms might be bounced back to the surface by the ambient gas. Such a phenomenon has been observed in our ongoing large-scale one-dimensional shock wave modelling. An extreme extension would be that when the molecular mass of ambient gas is infinitely large, some ejected target atoms will penetrate the ambient gas while others will hit the ambient

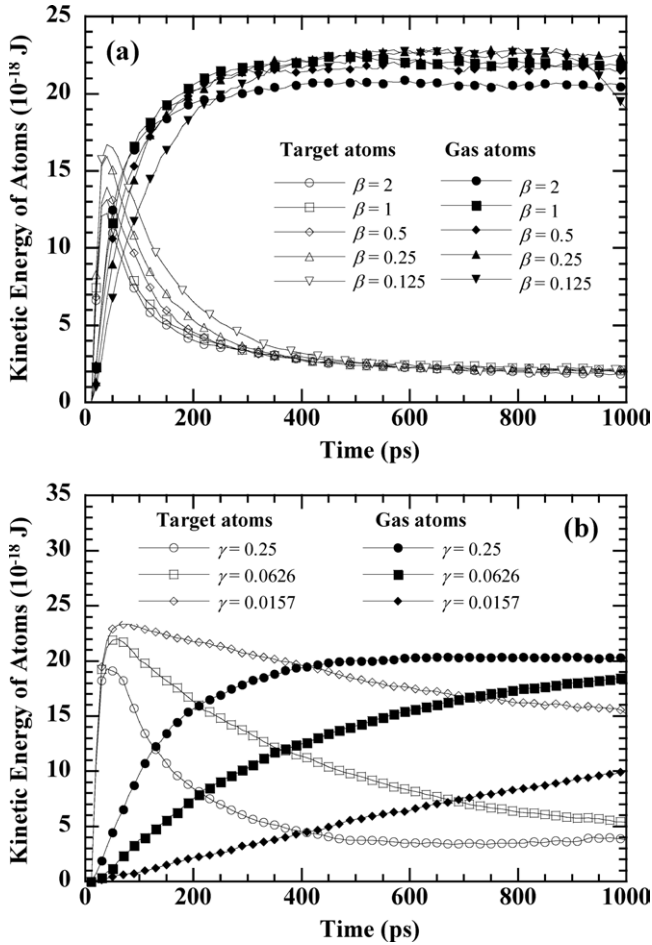


Figure 8. Kinetic energy of ejected atoms and kinetic energy change of ambient gas atoms: (a) under different molecular mass ratios ($\gamma = 1$); (b) under different gas pressures ($\beta = 1$).

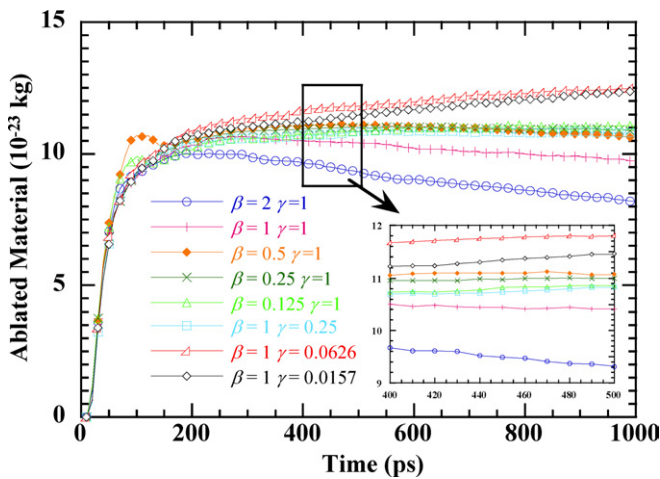


Figure 9. Material ablated under the influence of different β and γ .

gas and be reflected back. This will definitely give rise to the late stage ablation decay. In the other 3 lighter ambient gases, although the movement of ejected atoms is slowed down by the environment atoms, the bulk movement does not change direction. As a consequence, the material ablation in ($\beta = 0.5, \gamma = 1$), ($\beta = 0.25, \gamma = 1$) and ($\beta = 0.125, \gamma = 1$) are

higher than in ($\beta = 2, \gamma = 1$) and ($\beta = 1, \gamma = 1$). Under the influence of different γ , it is observed when the pressure is lower (smaller γ), more material will be ablated out due to the less constraint from the ambience. The ablated material is already very close to the ablation limit in vacuum for cases ($\beta = 1, \gamma = 0.0626$) and ($\beta = 1, \gamma = 0.0157$), so in figure 9 the difference between these two curves is very close ($\sim 5\%$ difference).

Mendes and Vilar experimentally investigated the influence of ambient gas on the ablation rate at large scales [28]. The material they used is $\text{Al}_2\text{O}_3\text{-TiC}$ ceramic whose average molecular weight is calculated as 84.3 g mol^{-1} . Their study showed that comparing with the ablation rate at 1 bar in Kr ($\beta = 1, \gamma = 1$), the ablation rate increased 21.7% in Ar ($\beta = 0.48, \gamma = 1$) and 65.2% in Ne ($\beta = 0.24, \gamma = 1$) [28]. In this work, the ablation rate increase with respect to the case ($\beta = 1, \gamma = 1$) is 9.5% for the case ($\beta = 0.5, \gamma = 1$) and 11.5% for the case ($\beta = 0.25, \gamma = 1$) at 2.17 bar. In Kr ambient gas, comparing with the ablation rate at 1 bar, the ablation rate increases 58.3% at 0.25 bar ($\gamma = 0.25$), 75.0% at 0.0626 bar ($\gamma = 0.0626$) and 83.3% at 0.0157 bar ($\gamma = 0.0157$). The ablation rate calculated in this work, comparing with case ($\beta = 1, \gamma = 1$), increases 10.8% for case ($\beta = 1, \gamma = 0.25$), 28.1% for case ($\beta = 1, \gamma = 0.0626$) and 26.8% for case ($\beta = 1, \gamma = 0.0157$). The difference between the experiment and the MD simulation about the effect of the molecular weight and ambient pressure is probably due to the laser ablation conditions. The MD simulation of this work is focused on nanoscale (4 nm diameter at e^{-1}) surface laser ablation using a picosecond laser pulse (5 ps FWHM) while the experiment reported in [28] is for nanosecond laser ablation (30 ns FWHM) with a laser spot of $250 \mu\text{m}$. Nevertheless, both the experiment and the MD simulation indicate the same trend for the effect of the molecular weight and pressure of the ambient gas.

4. Conclusion

In this work, quasi three-dimensional systems with over 2 million atoms were simulated using parallel MD simulation. Detailed studies were carried out about the shock wave front and Mach numbers, evolution of plume and ambient gas interaction zone and energy exchange between the ambient gas and plume. The plume affected a larger area under lower ambient pressure or lighter ambient gas, while the strength of the shock wave front was weaker since the diameter of the plume was larger. It was observed with the same ambient pressure and laser fluence that the ablated material will feature the same kinetic energy at the late stage regardless of the molecular weight of the ambient gas. The same conclusion holds for the energy increase of the ambient gas as well. When the ambient pressure was reduced, more kinetic energy was carried out by the ablated material while less energy was transferred to the ambient gas. By studying the ablation change with time, it was observed that when a heavier ambient gas was present, the ablated material could be bounced back by the ambient atoms.

Acknowledgment

Support for this work from Iowa State University through the start-up fund is gratefully acknowledged. This work is partially supported by ONR through the MURI program and by NSF (CMMI: 0820747).

References

- [1] Kohler M and Freitzsche W 2004 *Nanotechnology: An Introduction to Nanostructuring Techniques* (Weinheim: Wiley-VCH)
- [2] Lu Y F, Hu B, Mai Z H, Wang W J, Chim W K and Chong T C 2001 *Japan. J. Appl. Phys.* **40** 4395–8
- [3] Jersch J, Demming F and Dickmann K 1997 *Appl. Phys. A* **64** 29–32
- [4] Lu Y F, Mai Z H, Zheng Y W and Song W D 2000 *Appl. Phys. Lett.* **76** 1200–2
- [5] Jersch J and Dickmann K 1996 *Appl. Phys. Lett.* **68** 868–70
- [6] Jersch J, Demming F, Hildenhagen L J and Dickmann K 1998 *Appl. Phys. A* **66** 29–34
- [7] Lu Y F, Mai Z H, Qiu G and Chim W K 1999 *Appl. Phys. Lett.* **75** 2359–61
- [8] Hu B, Lu Y F, Mai Z H, Song W D and Chim W K 2000 *1st Int. Symp. on Laser Precision Microfabrication (Omiya, Saitama, Japan)* pp 232
- [9] Mai Z H, Lu Y F, Huang S M, Chim W K and Pan J S 2000 *J. Vac. Sci. Technol. B* **18** 1853–7
- [10] Mai Z H, Lu Y F, Song W D and Chim W K 2000 *Appl. Surf. Sci.* **360** 154–5
- [11] Saiki T and Narita Y 2002 *JSAP Int.* **5** 22–9
- [12] Jin E X and Xu X F 2005 *J. Quant. Spectrosc. Radiat. Transfer* **93** 163–73
- [13] Wang L, Jin E X, Uppuluri S M and Xu X F 2006 *Opt. Express* **14** 9902
- [14] Fang N, Lee H, Sun C and Zhang X 2005 *Science* **308** 534–7
- [15] Lu Y F, Mai Z H and Chim W K 1999 *Japan. J. Appl. Phys.* **38** 5910–5
- [16] Chimmalgi A, Choi T and Grigoropoulos C P 2002 *ASME International Mechanical Engineering Congress and Exposition (New Orleans, LA)* pp 291–5
- [17] Huang S M, Hong M H, Lu Y F, Lukyanchuk B S, Song W D and Chong T C 2002 *J. Appl. Phys.* **91** 3268–74
- [18] Porneala C and Willis D A 2006 *Appl. Phys. Lett.* **89** 211121–3
- [19] Zhang Z and Gogos G 2004 *Phys. Rev. B* **69** 235403–9
- [20] Jeong S H, Greif R and Russo R E 1999 *J. Phys. D: Appl. Phys.* **32** 2578–85
- [21] Kohen D and Martens C C 1999 *J. Chem. Phys.* **111** 4343–50
- [22] Wang X 2005 *J. Phys. D: Appl. Phys.* **38** 1805
- [23] Wang X and Lu Y 2005 *J. Appl. Phys.* **98** 114304–10
- [24] Feng X and Wang X 2007 *Phys. Lett. A* **369** 323–7
- [25] Allen M P and Tildesley D J 1987 *Computer Simulation of Liquids* (Oxford: Clarendon)
- [26] Feng X and Wang X 2008 *Appl. Surf. Sci.* **254** 4201–10
- [27] Edens A D, Ditmire T, Hansen J F, Edwards J F, Adams R G, Rambo P, Ruggles L, Smith I C and Porter J L 2004 *Phys. Plasmas.* **11** 4968–72
- [28] Mendes M and Vilar R 2003 *Appl. Surface Sci.* **206** 196–208